

X-ray sources in the starburst spiral galaxy M 83

Nuclear region and discrete source population

R. Soria^{1,2} and K. Wu^{1,2}

¹ Mullard Space Science Laboratory, University College London, Holmbury St Mary, Surrey RH5 6NT, UK
e-mail: kw@mssl.ucl.ac.uk

² School of Physics A28, University of Sydney, NSW 2006, Australia

Received 18 October 2001 / Accepted 4 January 2002

Abstract. *Chandra* has resolved the starburst nuclear region of the face-on grand-design spiral M 83. Eighty-one point sources are detected (above 3.5σ) in the ACIS S3 image, and 15 of them are within the inner $16''$ region of the galaxy. A point source with $L_x \approx 3 \times 10^{38}$ erg s⁻¹ in the 0.3–8.0 keV band is found to coincide with the infra-red nuclear photometric peak, one of the two dynamical nuclei of the galaxy. No point-like sources are resolved (at a 2.5σ level) at the centre of symmetry of the outer optical isophote ellipses, suspected to be another dynamical nucleus. About 50% of the total emission in the nuclear region is unresolved; of this, about 70% can be attributed to hot thermal plasma, and the rest is probably due to unresolved point sources (e.g., faint X-ray binaries). The azimuthally-averaged radial distribution of the unresolved emission has a King-like profile, with no central cusp. Strong emission lines are seen in the spectrum of the optically thin plasma component. The high abundances of C, Ne, Mg, Si and S with respect to Fe suggest that the interstellar medium in the nucleus is enriched and heated by type-II supernova explosions and winds from massive stars. The cumulative luminosity distribution of the discrete X-ray sources is neither a single nor a broken power law. Separating the sources in the nuclear region (within a distance of $60''$ from the X-ray centre) from the rest reveals that the two groups have different luminosity distributions. The $\log N(>S) - \log S$ curve of the sources in the inner region (nucleus and stellar bar) is a single power law, which we interpret as due to continuous, ongoing star formation. Outside the central region, there is a smaller fraction of sources brighter than the Eddington limit for an accreting neutron star.

Key words. galaxies: individual: M 83 (= NGC 5236) – galaxies: nuclei – galaxies: spiral – galaxies: starburst – X-rays: binaries – X-rays: galaxies

1. Introduction

M 83 (NGC 5236) is a grand-design, barred spiral galaxy (Hubble type SAB(s)c) with a starburst nucleus. Distance estimates are still very uncertain. A value of 3.7 Mpc was obtained by de Vaucouleurs et al. (1991). This places the galaxy in the Centaurus A group, whose members have a large spread in morphology and high velocities, indicating that the group is not virialised and tidal interactions and merging are frequent (de Vaucouleurs 1979; Côté et al. 1997). A distance of 8.9 Mpc was instead given in Sandage & Tamman (1987).

Infra-red (IR) observations (Gallais et al. 1991; Elmegreen et al. 1998; Thatte et al. 2000) have shown that the nuclear region of M 83 has a complex structure. From measurements of line-of-sight stellar velocities in the inner galactic region, two dynamical centres are inferred. The first centre is identified with a strong point-like optical/IR source. The second centre, located $1''.5$ to the South

and $3''.0$ to the West of the IR peak, is not associated with any bright source, but is approximately coincident with the centre of symmetry of the outer isophote ellipses. The stellar velocity dispersion implies that each dynamical centre contains an enclosed mass of $\approx 1.3 \times 10^7 M_\odot$ (Thatte et al. 2000).

The $J - K$ images of the nuclear region (Elmegreen et al. 1998) show two circumnuclear dust rings. The inner one has a radius of $2''.8$ and is centred on the IR nuclear peak; the outer one has a radius of $8''.6$ and is centred $2''.5$ South-West of the IR nucleus. The two rings are connected by a mini bar, oriented almost perpendicularly to the main galactic bar. Starburst activity is concentrated in a semi-circular annulus located $\approx 7''$ South-West of the IR nucleus, just inside the South-West half of the outer dust ring (Elmegreen et al. 1998; Harris et al. 2001).

M 83 was observed in the X-ray bands by *Einstein* in 1979–1981 (Trinchieri et al. 1985), by *ROSAT* in 1992–1994, and by *ASCA* in 1994 (Okada et al. 1997). Thirteen point sources were found in the *ROSAT* PSPC image (Ehle et al. 1998) and 37 in the *ROSAT* HRI image. After

Send offprint requests to: R. Soria,
e-mail: rs1@mssl.ucl.ac.uk

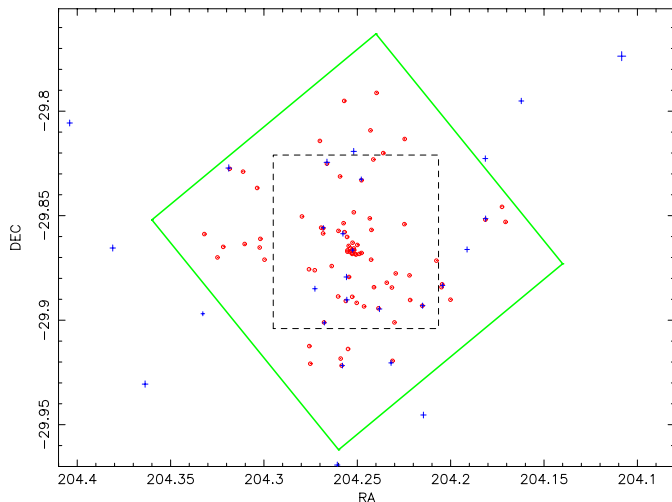


Fig. 1. Spatial distribution of the *Chandra* sources (red circles) detected in the S3 chip (green square), and of the *ROSAT* HRI sources (blue crosses with sizes denoting the positional uncertainty). The central region delimited by a dashed box is shown in greater detail in Fig. 2.

removing probable foreground stars and background AGN, there are 21 sources within the D_{25} ellipse believed to belong to the galaxy (Immler et al. 1999). The nuclear region, which encloses approximately 25% of the total X-ray luminosity in the 0.1–2.4 keV band, was unresolved in the *ROSAT* images.

M83 was observed by *Chandra* in 2000 April, and the data became available to the public in mid-2001. In this paper we report the results of our analysis of the *Chandra* archival data. We discuss the source population in the galaxy and the properties of discrete sources and unresolved emission in the nuclear region.

2. Data analysis

The *Chandra* observation was carried out on 2000 April 29 (Observation ID: 793; PI: G. Rieke), with the ACIS-S3 chip at the focus and a total exposure time of 50.978 ks. After screening out observational intervals corresponding to background flares, we retained a good time interval of 49.497 ks. The CXC CIAO software (version 2.2) was used in the analysis.

Discrete X-ray sources were identified using the CIAO source-finding routine *celldetect*. The percentage of the PSF energy encircled by the detect cells was chosen to be 80% at 1.5 keV. We did not select a higher percentage in order to avoid confusion of close-by sources in the nuclear region and of a few off-centre close pairs (e.g., the *ROSAT* HRI source H17, Immler et al. 1999). We compared the results obtained with *celldetect* with those obtained by using *wavdetect*, and we found no significant differences for sources away from the galactic centre, for a signal-to-noise ratio >3.5 . The routine *celldetect*, however, seems more successful at resolving the nuclear sources. Exposure maps at energies of 1.0, 1.7 and 3.0 keV were first calculated, and then used in the routine *dmextract* to correct the net count rates of the sources.

3. Global properties of the sources

A total of 81 point sources are detected in the S3 chip at a $3.5\text{-}\sigma$ level in the 0.3–8.0 keV band. Their positions, with an uncertainty of $0''.5$, their total photon counts and their counts in three separate energy bands (0.3–1.0 keV, 1.0–2.0 keV and 2.0–8.0 keV) are listed in Table A.1. The positions of the *ROSAT* sources given in Table 3 of Immler et al. (1999) have a systematic offset $\Delta(\text{RA}) \simeq -0''.5$ and $\Delta(\text{Dec}) \simeq 3''.5$ with respect to the *Chandra* S3 source positions. Therefore, we shifted the positions of the *ROSAT* sources by the same amount (without applying any rotation), before comparing them with the *Chandra* sources, as shown in the spatial distribution plot (Fig. 1).

Fifteen of the 18 *ROSAT* HRI sources within the field of view of the *Chandra* S3 chip are detected again. *Chandra* has resolved at least 15 sources in the nuclear region, which was not resolved in *ROSAT* HRI and PSPC images. It has also resolved two off-centre close pairs: the *ROSAT* HRI sources H12 and H27. The *ROSAT* HRI sources H11, H18 and H28 were undetected at a $2.5\text{-}\sigma$ level. If we assume an absorbing column density $n_{\text{H}} = 4 \times 10^{20} \text{ cm}^{-2}$ (the Galactic foreground absorption, from Schlegel et al. 1998 and Predehl & Schmitt 1995) and a power-law spectrum with photon index $\Gamma = 1.5$ for all the sources, the detection threshold of $\simeq 15$ net counts places an upper limit of $f_{\text{x}} \simeq 2.0 \times 10^{-15} \text{ erg cm}^{-2} \text{ s}^{-1}$ for the observed flux in the 0.3–8.0 keV band. Those three transients were therefore at least an order of magnitude fainter than they were during the *ROSAT* observations.

Most of the sources are concentrated in the nuclear region (Figs. 1, 2). Comparing the position of the *Chandra* S3 sources with a VLT *B* image shows that the off-centre sources tend to associate with the spiral arms (Fig. 2, top panel). The sources have a large spread in the hardness of their X-ray emission. A “true-colour” X-ray image of the nuclear region is shown in Fig. 2, bottom panel.

Separating the sources inside and outside a circular region of radius $60''$ from the geometric centre of the X-ray emission reveals that the two groups have different luminosity distributions in the 0.3–8.0 keV band. (A linear separation of $60''$ corresponds to 1.1 kpc for a distance of 3.7 Mpc, and is roughly half of the total length of the major galactic bar.) The cumulative $\log N(>S) - \log S$ distribution (where S are the photon counts) of the sources outside the circular inner region is neither a single nor a broken power law (Fig. 3). It shows a kink at $S \approx 250$ cts; the slope of the curve above this feature is -1.3 , while it is -0.6 at the faint end. The $\log N(>S) - \log S$ curve of the inner sources can instead be described as a single power law, with a slope of -0.8 . At an assumed distance of 3.7 Mpc, 100 counts ($\simeq 2.0 \times 10^{-3} \text{ cts s}^{-1}$) correspond to an unabsorbed source luminosity $L_{\text{x}} = 2.3 \times 10^{37} \text{ erg s}^{-1}$ in the 0.3–8.0 keV band. The kink in the $\log N(>S) - \log S$ curve of the sources outside the $60''$ circle is therefore located at $L_{\text{x}} \approx 6 \times 10^{37} \text{ erg s}^{-1}$ (0.3–8.0 keV band).

Some of the sources are likely to be background AGN. In order to investigate the effect of this correction, we have

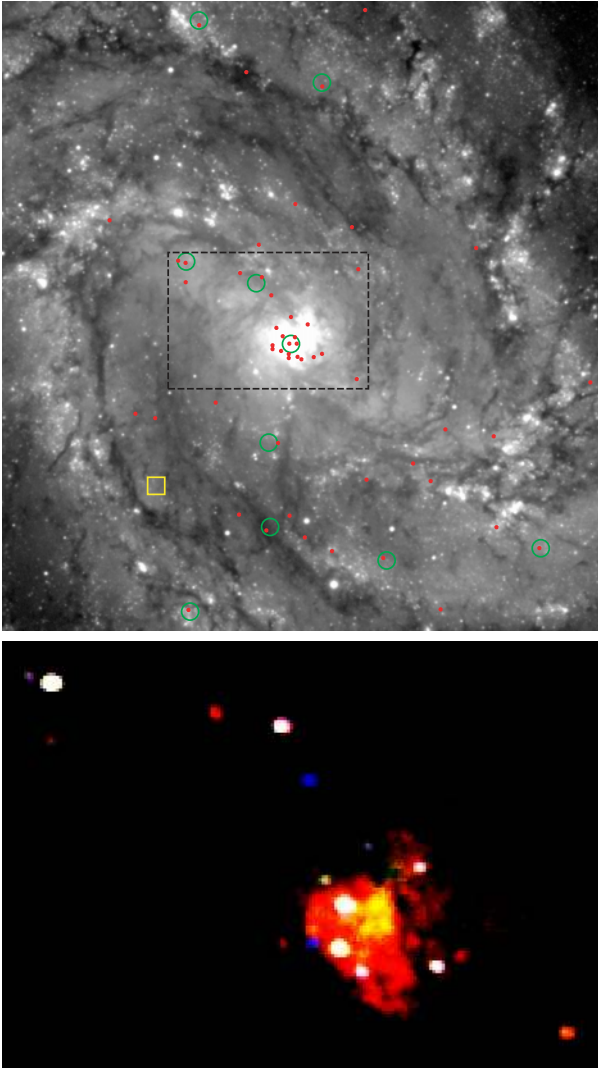


Fig. 2. Top panel: positions of the discrete X-ray sources overplotted on a Very Large Telescope (VLT) B image (inner $4'8 \times 5'0$ region of M83, including the main bar). The image was obtained from the ESO public archive; it was taken on 1999 March 11 with the FORS1 camera at Unit Telescope 1. The *Chandra* sources are represented by red circles (radius = $1''$), *ROSAT* sources detected by *Chandra* by green circles (radius = $4''$), and a *ROSAT* source not detected by *Chandra* by a yellow box (size = $8'' \times 8''$). Bottom panel: “true-colour” image of the nuclear region (delimited by the dashed box in the VLT B image), smoothed using a $1'5 \times 1'5$ boxcar kernel. Red, green and blue correspond to emission in the 0.3–1.0 keV, 1.0–2.0 keV and 2.0–8.0 keV bands respectively. In both images, North is up and East is left.

constructed the $\log N(>S) - \log S$ curves in a soft (0.5–2.0 keV) and hard (2.0–10.0 keV) band separately, and we have used the luminosity functions of faint background sources in the two bands, deduced from the Deep Field South survey (Giacconi et al. 2001). We find that about 15% of the sources are background AGN; the expected number in the inner $60''$ circle is smaller than one. The kink in the $\log N(>S) - \log S$ curve for the outer sources and the values of the slope at both ends are unaffected by the background subtraction. Because of the uncertainty

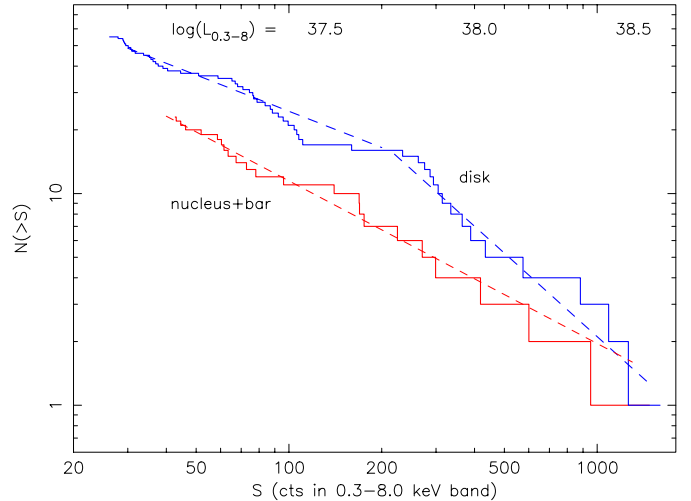


Fig. 3. The cumulative luminosity distributions of sources found in the 0.3–8.0 keV band is different for the population inside the $60''$ inner circle (which includes the starburst nuclear region and the main bar) and for the population outside of it (red and blue curves respectively). We interpret the single power-law distribution of the nuclear sources as evidence of continuous, ongoing star formation. The relative scarcity of bright sources in the disk population suggests that star formation is less active there. See Sect. 3 for the conversion from counts to luminosity.

in the distant AGN counts in different sky regions, the background correction itself is also uncertain; however, it is unlikely that anisotropic effects will significantly alter the results that we have presented above.

The number density of sources is about 7 kpc^{-2} in the inner $60''$ circular region, and is only 0.7 kpc^{-2} elsewhere in the S3 field, without any background subtraction. After the background sources are subtracted, the number density of the sources detected in the 0.3–8.0 keV band is 6 kpc^{-2} inside the circle and 0.6 kpc^{-2} outside. The source concentration is thus at least 10 times higher in the inner $60''$ ($\approx 1 \text{ kpc}$) than elsewhere in the galaxy.

4. Nuclear region

The nuclear region of M83 had not been clearly resolved in X-ray imaging observations (see e.g., the *ROSAT* HRI image, Immler et al. 1999) before *Chandra*. The *Chandra* data now reveal that M83 has a very highly structured nuclear region (Fig. 2, bottom panel, and Fig. 4). Fifteen discrete sources are detected within a radius of $\approx 16''$ ($\approx 290 \text{ pc}$) from the centre of symmetry of the outer optical isophotes. There are also clump-like features in the predominantly soft unresolved emission, which may be due to faint point sources or hot gas clouds. The strongest X-ray emission comes from an approximately circular region, with a radius of $\approx 7''$ and a geometrical centre at RA (2000) = $13^{\text{h}}37^{\text{m}}00^{\text{s}}.8$, Dec (2000) = $-29^{\circ}51'59''.3$. The region is inside the outer dust ring (Elmegreen et al. 1998), and it contains both the IR photometric nucleus (to the North-East) and the star-forming ring (to the South-West). The centre of the circle is less than $2''$ away from

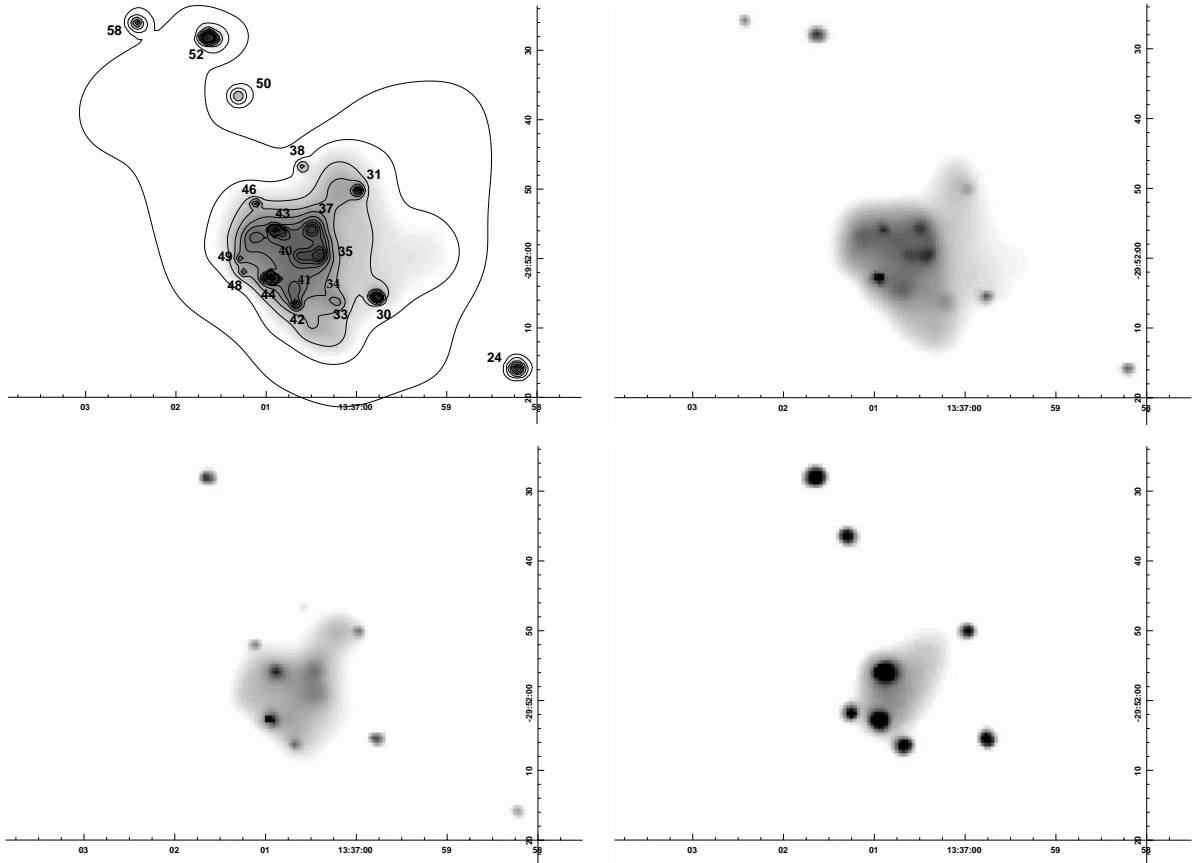


Fig. 4. Top left: image of the nuclear region of M 83 in the 0.3–8.0 keV band, with the contours of the X-ray emission overplotted in square-root scale; the numbers identify the sources listed in Table A.1. Top right: image in the 0.3–1.0 keV band, showing extended emission to the West of the star-forming arc. Bottom left: image in the 1.0–2.0 keV band. Bottom right: image in the 2.0–8.0 keV band. All images have been adaptively smoothed (CIAO task *csmooth*, with minimum signal-to-noise ratio = 4).

the invisible dynamical nucleus and the geometrical centre of the outer dust ring. The soft (0.3–1.0 keV) unresolved emission is more spatially extended than the hard (2.0–8.0 keV) emission (Fig. 4).

We removed the point sources using the extraction regions from *celldetect* (see Sect. 2) and extracted counts from concentric annuli to construct radial brightness profiles of the unresolved emission in the nuclear region. We have found that the brightness is approximately constant in a circular region up to a radius of $7''$ and then declines radially with a power-law like profile (Fig. 5). Single power-law and Gaussian profiles do not provide acceptable fits to the azimuthally-averaged profile. Better fits are obtained using a King profile, yielding a core radius of $6''.7 \pm 0''.5$ (≈ 120 pc), and a power law with a slope of -1.9 ± 0.2 beyond the core.

The brightness distribution is not axisymmetric. If we divide the region into four different quadrants, defined by taking the directions parallel and perpendicular to the main stellar bar (which has a position angle = $51^\circ 7'$), the brightness is found to drop more steeply East of the nucleus and the emission is more extended to the West (Fig. 5). The difference in the brightness profiles of the four quadrants is in fact mainly due to the extended emission region westward of the star-forming arc. We have also

examined the radial brightness profiles obtained by choosing various other reference centres (e.g., the two dynamical nuclei inferred from IR observations), but none of them appears simpler or more axisymmetric.

We extracted the spectrum of the unresolved emission inside the inner $16''$ circle, excluding the resolved point sources, and we fitted it using an absorbed, single-temperature vmekal plus power-law model (XSPEC, version 11.0.1, Arnaud 1996). Assuming solar abundances, we obtain the best-fit parameters listed in Table 1 (“model 1”). The predicted lines are not strong enough to account for the data, leading to poor fit statistics ($\chi^2_\nu = 1.42$, 114 d.o.f.). Increasing the abundance of all the metals by the same constant factor does not improve the χ^2_ν .

We then assumed a different set of abundances (Table 1, “model 2”), and fitted again a vmekal plus power-law model to the spectrum of the unresolved emission. Our choice of higher abundances for C, Ne, Mg, Si and S relative to Fe is physically justified if the interstellar medium has been enriched by type-II supernova ejecta and winds from very massive, young stars (see also Sect. 6.2). For this set of abundances, the model gives a total (i.e., Galactic foreground plus intrinsic) absorption column density $n_{\text{H}} = (1.1^{+0.2}_{-0.3}) \times 10^{21} \text{ cm}^{-2}$,

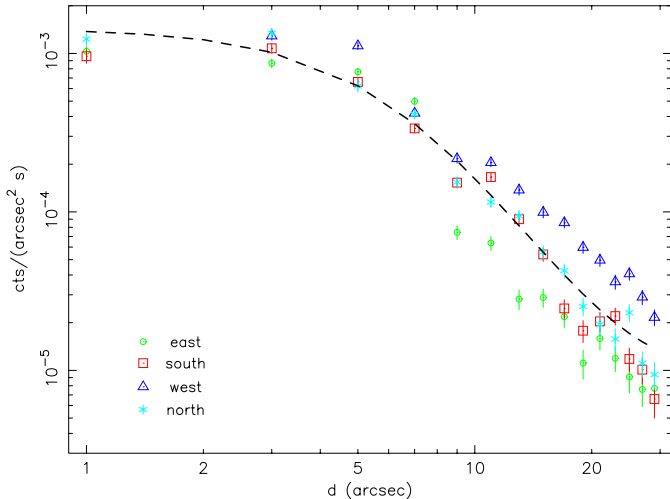


Fig. 5. Radial profiles of the X-ray surface brightness in the nuclear region, centred at RA (2000) = $13^{\text{h}}37^{\text{m}}00^{\text{s}}.8$, Dec (2000) = $-29^{\circ}51'59''.3$. The profiles in the North, South, East and West quadrants are represented by light blue asterisks, red squares, green circles and blue triangles respectively. The best-fit King model (dashed line) for the azimuthally-averaged radial brightness profile is also shown to illustrate the relative anisotropy.

temperature $kT = (0.58_{-0.02}^{+0.03})$ keV, and power-law photon index $\Gamma = 2.7_{-0.3}^{+0.3}$ ($\chi^2_{\nu} = 0.99$, 114 d.o.f.). In any case, the absorption column density, thermal plasma temperature and power-law photon index are only weakly dependent on the precise abundances.

We left the redshift as a free parameter in our spectral fitting. We obtain that the emission lines are redshifted, with projected radial velocities ≈ 7000 km s $^{-1}$, also almost independent of the choice of metal abundances. This is far in excess of the systemic radial velocity of M83 ($v_r = 505$ km s $^{-1}$, Tilanus & Allen 1993). A spatially resolved determination of the hot gas dynamics is left to further work.

We have also calculated the total (resolved plus unresolved) luminosity from the circular regions within radii of $7''$ (this is approximately the region inside the outer dust ring) and $16''$ from the geometric centre of the X-ray emission, using an absorbed, optically-thin thermal plasma plus power-law model. The total emitted luminosity in the 0.3–8.0 keV band is $\simeq 15.7 \times 10^{38}$ erg s $^{-1}$ inside $7''$ and $\simeq 23.8 \times 10^{38}$ erg s $^{-1}$ inside $16''$ (Table 2). Discrete sources contribute $\simeq 50\%$ of the total luminosity.

The unresolved emission is itself the sum of truly diffuse emission from optically thin gas, and emission from unresolved point-like sources (e.g., faint X-ray binaries). Assuming that the latter contribution is responsible for the power-law component in the spectrum of the unresolved emission, we estimate that emission from truly diffuse thermal plasma contributes $\simeq 35\%$ of the total luminosity (Table 2).

Extrapolating the $\log N(>S) - \log S$ curve for the nuclear sources (see Sect. 3) gives us another way of estimating the relative contribution to the unresolved emission of truly diffuse gas and faint point-like sources.

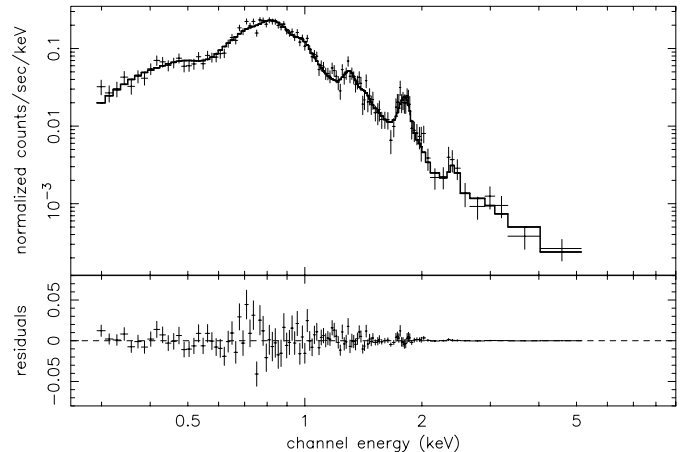


Fig. 6. The spectrum of the unresolved emission in the nuclear region (inside a $16''$ circle) shows very strong emission lines from Mg XI (1.33–1.35 keV), Si XIII (1.84–1.87 keV) and S XV (2.43 keV). The other major contributions to the spectrum come from C VI (0.37–0.44 keV), O VII (triplet, 0.56–0.57 keV), Ne IX (triplet, 0.91–0.92 keV), Ne X (1.02 keV), and the Fe XVII L-line complex (0.6–0.9 keV). The spectrum is well fitted by an absorbed, single-temperature vemkal plus power-law model; the fit parameters are listed in Table 1 (“model 2”). The background-subtracted spectrum has been grouped to achieve a S/N ratio ≥ 3 for each bin.

Table 1. Parameters used in the model spectral fits for the unresolved emission in the inner $16''$, with two different sets of abundances.

model: $\text{tbabs}_{\text{Gal}} \times \text{tbabs} \times (\text{power-law} + \text{vmekal})$		
parameter	model 1	model 2
$n_{\text{H}} (\times 10^{21} \text{ cm}^{-2})$	$1.6_{-0.3}^{+0.3}$	$1.1_{-0.3}^{+0.2}$
Γ	$3.1_{-0.2}^{+0.1}$	$2.7_{-0.3}^{+0.3}$
$K_{\text{pl}} (\times 10^{-5})$	$7.6_{-0.9}^{+1.5}$	$3.9_{-0.9}^{+0.8}$
T (keV)	$0.60_{-0.03}^{+0.02}$	$0.58_{-0.02}^{+0.03}$
$K_{\text{vm}} (\times 10^{-5})$	$13.7_{-0.6}^{+2.0}$	$12.5_{-1.2}^{+0.8}$
V_r (km s $^{-1}$)	5980_{-1470}^{+4770}	7270_{-2310}^{+1900}
C (fixed)	1.0	10.0
N (fixed)	1.0	1.0
O (fixed)	1.0	1.0
Ne (fixed)	1.0	2.0
Na (fixed)	1.0	1.0
Mg (fixed)	1.0	2.5
Al (fixed)	1.0	1.0
Si (fixed)	1.0	3.0
S (fixed)	1.0	3.0
Ar (fixed)	1.0	1.0
Ca (fixed)	1.0	1.0
Fe (fixed)	1.0	0.9
Ni (fixed)	1.0	1.0
χ^2_{ν} (d.o.f.)	1.42 (114)	0.99 (114)

We obtain that unresolved point-like X-ray sources brighter than 10^{34} erg s $^{-1}$ would contribute $\approx 4.2 \times 10^{38}$ erg s $^{-1}$ to the luminosity in the inner $60''$ region. Of the 23 discrete sources identified within the $60''$ radius, 15 are found within the inner $16''$. Assuming that

Table 2. Luminosity of emission from discrete and unresolved sources in the nuclear region (0.3–8.0 keV band).

luminosity ($\times 10^{38}$ erg s $^{-1}$)	inside 7''	inside 16''
discrete sources	7.7	12.3
unresolved sources	8.0	11.5
optically-thin thermal component	5.5	7.8
power-law component	2.5	3.7
total	15.7	23.8

the same uniform scaling applies to the emission of both resolved and unresolved stellar sources, this implies that unresolved point-like sources inside 16'' would have a total luminosity of $\approx 2.7 \times 10^{38}$ erg s $^{-1}$.

Another possible contribution to the unresolved emission detected inside the inner 16'' comes from photons emitted by the resolved sources but falling outside the extraction regions, in the wings of the PSF. Taking into account the partial spatial overlapping of the detection cells, we estimate that this contribution is $\lesssim 1.5 \times 10^{38}$ erg s $^{-1}$.

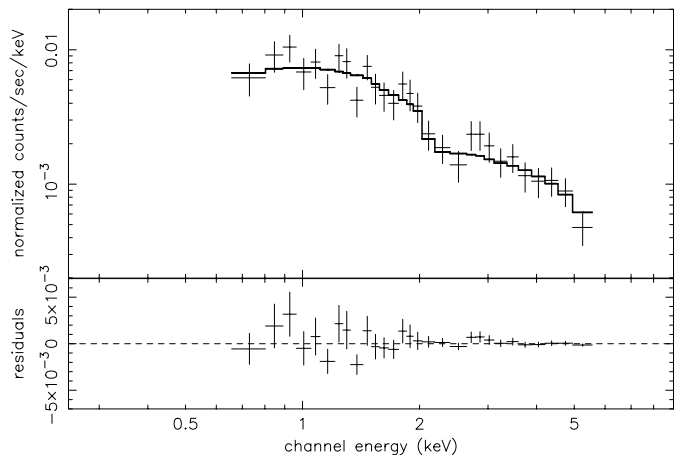
Thus, the combined contribution of faint X-ray sources and emission in the wings of the PSF can account for the power-law component inferred from the spectral fitting of the unresolved emission (Table 2). This also confirms that a substantial proportion ($\approx 70\%$) of the unresolved emission is indeed due to truly diffuse gas rather than faint point-like sources.

5. Spectral properties of three bright sources

The true-colour X-ray image of the nuclear region (Fig. 2, bottom panel) and the soft- and hard-band images in Fig. 4 clearly show the variations of spectral properties among the discrete sources and the different spatial distributions for the soft and hard emission. Although a more detailed analysis of the discrete sources will be presented in a future paper (Soria et al., in preparation), here we briefly discuss the spectral properties of the two brightest nuclear sources (Nos. 43 and 44 in Table A.1). For comparison, we also present the *Chandra* spectrum of the brightest source in the galaxy, the *ROSAT* HRI source H30 (an off-centre source located outside the S3 field of view).

5.1. Two bright nuclear sources

Sources Nos. 43 and 44 are the two brightest nuclear sources in the 0.3–8.0 keV band (Table A.1). The IR photometric nucleus (source No. 43) is embedded in strong diffuse emission from optically thin plasma, which reduces the precision with which we can determine its spectral parameters. We extracted the source and the background spectra using the routine *psextract* in CIAO and fitted the background-subtracted spectrum (Fig. 7) using standard models in XSPEC. The spectrum is well fitted ($\chi^2_\nu = 0.8$, 26 d.o.f.) by an absorbed power-law model, with a

**Fig. 7.** Spectrum of the IR photometric nucleus (source No. 43 in Fig. 4 and Table A.1). The model spectrum (solid line) is an absorbed power law, and the best-fit parameters are listed in Table 3. The background-subtracted spectrum has been grouped to achieve a S/N ratio ≥ 4 in each bin.

total column density $n_{\text{H}} = (1.0^{+1.4}_{-0.6}) \times 10^{21}$ cm $^{-2}$ and a power-law photon index $\Gamma = (1.15^{+0.18}_{-0.22})$ (Table 3). The implied emitted luminosity for a distance of 3.7 Mpc is $L_{\text{x}} = 2.6 \times 10^{38}$ erg s $^{-1}$ in the 0.3–8.0 keV band, which is slightly higher than the Eddington luminosity of a $1.5-M_{\odot}$ accreting compact object.

Source No. 44 has the highest count rate among all discrete nuclear sources. It is located about 7'' South of the IR photometric nucleus, and is near the southern end of the star-forming ring. The source and background spectra were again extracted with *psextract*. A simple absorbed power-law model provides a good fit ($\chi^2_\nu = 1.02$, 53 d.o.f.), with total column density $n_{\text{H}} = (1.9^{+0.4}_{-0.4}) \times 10^{21}$ cm $^{-2}$ and power-law photon index $\Gamma = (2.7^{+0.2}_{-0.2})$ (Fig. 8 and Table 4). The deduced emitted luminosity is $L_{\text{x}} \simeq 4.6 \times 10^{38}$ in the 0.3–8.0 keV band.

In fact, this choice of spectral model may over-estimate the true column density and luminosity, if the spectrum turns over at low energies. Therefore, we also fitted the spectrum with the *bmc* model in XSPEC, which consists of a black-body component and a hard, power-law-like tail produced by Comptonisation of the soft photons by high energy electrons (e.g., Shrader & Titarchuk 1999). We obtain an equally good fit ($\chi^2_\nu = 1.02$, 52 d.o.f.) with the following parameters: total column density $n_{\text{H}} = (0.9 \pm 0.1) \times 10^{21}$ cm $^{-2}$, temperature of the seed photons $kT = (0.16 \pm 0.08)$ keV, photon index of the power-law tail $\Gamma = (2.6^{+0.1}_{-0.1})$. For this model, the luminosity emitted in the 0.3–8.0 keV band is only $L_{\text{x}} \simeq 2.4 \times 10^{38}$.

5.2. ROSAT source H30

The source H30 is the brightest point source inside the M 83 D $_{25}$ ellipse; it is located at RA (2000) = 13^h37^m19^s.8, Dec (2000) = $-29^{\circ}53'48''.9$, which is about 4'.5 South-East of the nucleus. The source is in the S2 chip and therefore is not listed in Table A.1.

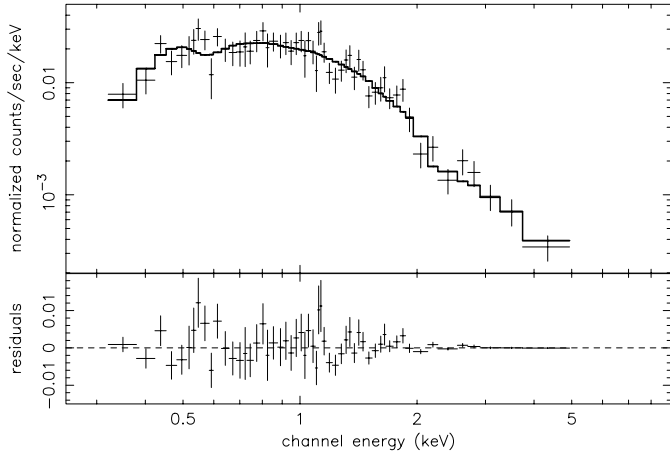


Fig. 8. Spectrum of source No. 44 in the nuclear region. The model spectrum (solid line) is an absorbed power law, and the best-fit parameters are listed in Table 4. The background-subtracted spectrum has been grouped to achieve a S/N ratio ≥ 4 .

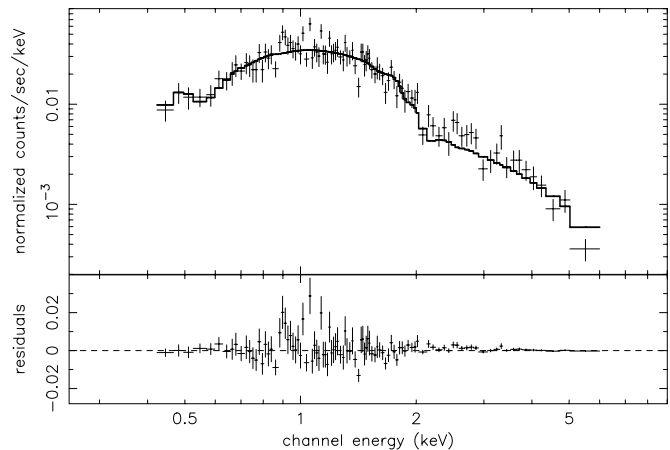


Fig. 9. Spectrum of the *ROSAT* HRI source H30. The model spectrum (solid line) is an absorbed power law, and the best-fit parameters are listed in Table 5. The background-subtracted spectrum has been grouped to achieve a S/N ratio ≥ 4 .

A model with a simple absorbed power law provides an acceptable fit ($\chi^2_\nu = 1.32$, 98 d.o.f.), with total absorption column density $n_{\text{H}} = (2.5^{+0.4}_{-0.3}) \times 10^{21} \text{ cm}^{-2}$ and power-law photon index $\Gamma = 2.45^{+0.13}_{-0.12}$ (Fig. 9 and Table 5). The implied emitted luminosity is $L_{\text{x}} \simeq 11 \times 10^{38} \text{ erg s}^{-1}$ in the 0.3–8.0 keV band.

As before, lower luminosities are obtained when the spectrum is fitted with a Comptonisation model including a soft blackbody component and a hard tail. Using *bmc* in *XSPEC*, we obtain an equally good fit ($\chi^2_\nu = 1.32$, 98 d.o.f.) with total $n_{\text{H}} = (4 \times 10^{20}) \text{ cm}^{-2}$ (fixed at the Galactic value with no intrinsic absorption), blackbody temperature $kT = (0.26^{+0.01}_{-0.01}) \text{ keV}$, and hard tail photon index $\Gamma = 2.45^{+0.06}_{-0.08}$ (Table 5). For this choice of model, the implied emitted luminosity is $L_{\text{x}} \simeq 5.6 \times 10^{38} \text{ erg s}^{-1}$ in the 0.3–8.0 keV band.

As a test, we then fitted the spectrum with a disk blackbody model, which also provides an acceptable fit ($\chi^2_\nu = 1.33$, 99 d.o.f.). The best-fit disk-blackbody

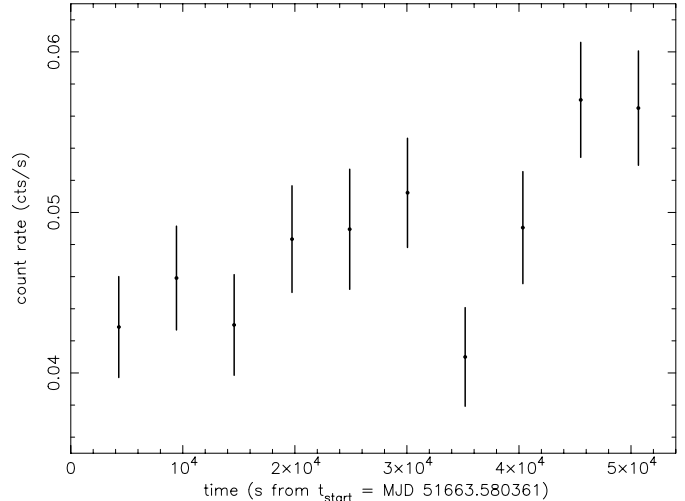


Fig. 10. The 0.3–8.0 keV band light-curve of the *ROSAT* HRI source H30 shows variability significant at the 90% level. The data are binned in 10 time intervals of approximately 5 ks each.

colour temperature $kT_{\text{in}} = (0.92^{+0.05}_{-0.04}) \text{ keV}$, the emitted luminosity $L_{\text{x}} \simeq 5.4 \times 10^{38} \text{ erg s}^{-1}$, and the other parameters are listed in Table 5.

Finally, we fitted the spectrum with a thermal bremsstrahlung model, which formally provides the best fit ($\chi^2_\nu = 1.23$, 99 d.o.f.). The fit parameters (Table 5) are in agreement, at $2\text{-}\sigma$ level, with those obtained by Immler et al. (1999). With this model, the emitted luminosity in the 0.3–8.0 keV band is $L_{\text{x}} \simeq 6.7 \times 10^{38} \text{ erg s}^{-1}$, corresponding to $L_{\text{x}} \simeq 5.5 \times 10^{38} \text{ erg s}^{-1}$ in the 0.1–2.4 keV band and $L_{\text{x}} \simeq 4.2 \times 10^{38} \text{ erg s}^{-1}$ in the 0.5–3.0 keV band. This is roughly consistent with the values of $6.7 \times 10^{38} \text{ erg s}^{-1}$ obtained from the *ROSAT* HRI data at 0.1–2.4 keV, $5.7 \times 10^{38} \text{ erg s}^{-1}$ obtained from the *Einstein* IPC data at 0.5–3.0 keV, and $4.2 \times 10^{38} \text{ erg s}^{-1}$ obtained from the *Einstein* HRI data also at 0.5–3.0 keV, for a distance of 3.7 Mpc (Immler et al. 1999; Trinchieri et al. 1985). We therefore conclude that the source does not show strong evidence of long-term X-ray variability.

The source appears to show an increase in brightness during the 50-ks *Chandra* observation (Fig. 10). Fitting a constant to the count rate, binned into ten 5-ks time intervals, yields $\chi^2_\nu = 2.7$ (9 d.o.f.), while a linear fit with $dS/dt = 2.4 \times 10^{-7} \text{ cts s}^{-2}$ gives $\chi^2_\nu = 1.6$ (8 d.o.f.). The $\Delta\chi^2$ indicates that the variability is significant at the 90% level. Short-term variabilities were also detected during the *ROSAT* observations (Immler et al. 1999).

6. Discussion

6.1. Luminosity distribution of the sources

Recent observations have shown that the luminosity distributions of X-ray sources in nearby galaxies can often be approximated by a power-law (e.g., disk sources in M101, Pence et al. 2001, and M81, Tennant et al. 2001) or by a broken power-law profile (e.g., bulge sources in M31, Shirey et al. 2001, and in M81, Tennant et al. 2001). The $\log N(>S) - \log S$ curves for the sources located in the

Table 3. XSPEC best-fit parameters for the X-ray source at the IR photometric nucleus (No. 43 in Table A.1). The foreground (Galactic) line-of-sight absorption column density has been fixed at $n_{\text{H,Gal}} = 4 \times 10^{20} \text{ cm}^{-2}$.

model: $\text{tbabs}_{\text{Gal}} \times \text{tbabs} \times \text{power-law}$	
$n_{\text{H}} (\times 10^{20} \text{ cm}^{-2})$	$5.6^{+14.2}_{-5.6}$
Γ	$1.15^{+0.18}_{-0.22}$
$K_{\text{pl}} (\times 10^{-5})$	$1.5^{+0.5}_{-0.3}$
χ^2_{ν} (d.o.f.)	0.80 (26)
$L_{0.3-8} (\times 10^{38} \text{ erg s}^{-1})$	2.6

Table 4. XSPEC best-fit parameters for the nuclear source No. 44. The foreground column density has been fixed at $n_{\text{H,Gal}} = 4 \times 10^{20} \text{ cm}^{-2}$.

model: $\text{tbabs}_{\text{Gal}} \times \text{tbabs} \times \text{power-law}$	
$n_{\text{H}} (\times 10^{20} \text{ cm}^{-2})$	$18.9^{+4.2}_{-4.0}$
Γ	$2.74^{+0.12}_{-0.20}$
$K_{\text{pl}} (\times 10^{-5})$	$5.9^{+1.0}_{-0.9}$
χ^2_{ν} (d.o.f.)	1.02 (53)
$L_{0.3-8} (\times 10^{38} \text{ erg s}^{-1})$	4.6
model: $\text{tbabs}_{\text{Gal}} \times \text{tbabs} \times \text{bmc}$	
$n_{\text{H}} (\times 10^{20} \text{ cm}^{-2})$	$4.9^{+0.9}_{-0.9}$
$T_{\text{bb}} (\text{keV})$	$0.16^{+0.08}_{-0.08}$
Γ	$2.59^{+0.14}_{-0.14}$
$K_{\text{bmc}} (\times 10^{-6})$	$1.1^{+0.6}_{-0.6}$
χ^2_{ν} (d.o.f.)	1.02 (52)
$L_{0.3-8} (\times 10^{38} \text{ erg s}^{-1})$	2.4

bulges of spiral galaxies tend to have steeper slopes at the high-luminosity end. For example, the broken power-law distribution for bulge sources in M31 has slopes of -0.5 and -1.8 at the low- and high-luminosity end, respectively (Shirey et al. 2001). The $\log N(>S) - \log S$ curves for the sources in galactic disks are generally single, flatter power laws (e.g., with a slope of -0.5 for the disk sources in M81, Tennant et al. 2001, and -0.8 for the disk sources in M101, Pence et al. 2001). Elliptical galaxies also have broken power-law $\log N(>S) - \log S$ curves, with generally steep slopes at their bright ends (e.g., with a slope of -1.8 for NGC 4697, Sarazin et al. 2000), similar to those inferred for the bulge sources in spiral galaxies. Starburst galaxies, instead, tend to have flat power-law $\log N(>S) - \log S$ curves (e.g., with a slope of -0.45 for NGC 4038, Fabbiano et al. 2001) similar to the distributions for the disk sources in spiral galaxies.

A flatter power-law luminosity distribution implies a larger proportion of bright sources in a population. If the brightest X-ray sources in a galaxy are young, short-lived high-mass X-ray binaries, born in a recent starburst episode, then the slope of the bright end of the $\log N(>S) - \log S$ curve indicates the star-formation activity of the galaxy (see Prestwich 2001).

Table 5. XSPEC best-fit parameters for the *ROSAT* HRI source H30. The foreground column density has been fixed at $n_{\text{H,Gal}} = 4 \times 10^{20} \text{ cm}^{-2}$.

model: $\text{tbabs}_{\text{Gal}} \times \text{tbabs} \times \text{power-law}$	
$n_{\text{H}} (\times 10^{21} \text{ cm}^{-2})$	$2.1^{+0.4}_{-0.3}$
Γ	$2.45^{+0.13}_{-0.12}$
$K_{\text{pl}} (\times 10^{-4})$	$1.38^{+0.16}_{-0.14}$
χ^2_{ν} (d.o.f.)	1.32 (98)
$L_{0.3-8} (\times 10^{38} \text{ erg s}^{-1})$	11
model: $\text{tbabs}_{\text{Gal}} \times \text{tbabs} \times \text{diskbb}$	
$n_{\text{H}} (\times 10^{21} \text{ cm}^{-2})$ (fixed)	0.0
$T_{\text{in}} (\text{keV})$	$0.92^{+0.05}_{-0.04}$
$K_{\text{dbb}} (\times 10^{-2})$	$2.25^{+0.47}_{-0.38}$
χ^2_{ν} (d.o.f.)	1.33 (99)
$L_{0.3-8} (\times 10^{38} \text{ erg s}^{-1})$	5.4
model: $\text{tbabs}_{\text{Gal}} \times \text{tbabs} \times \text{bmc}$	
$n_{\text{H}} (\times 10^{21} \text{ cm}^{-2})$ (fixed)	0.0
$T_{\text{bb}} (\text{keV})$	$0.26^{+0.01}_{-0.01}$
Γ	$2.45^{+0.06}_{-0.08}$
$K_{\text{bmc}} (\times 10^{-6})$	$2.4^{+0.2}_{-0.2}$
χ^2_{ν} (d.o.f.)	1.32 (98)
$L_{0.3-8} (\times 10^{38} \text{ erg s}^{-1})$	5.6
model: $\text{tbabs}_{\text{Gal}} \times \text{tbabs} \times \text{bremsstrahlung}$	
$n_{\text{H}} (\times 10^{21} \text{ cm}^{-2})$	$0.82^{+0.23}_{-0.22}$
$T_{\text{br}} (\text{keV})$	$2.56^{+0.32}_{-0.28}$
$K_{\text{br}} (\times 10^{-4})$	$1.29^{+0.13}_{-0.11}$
χ^2_{ν} (d.o.f.)	1.23 (98)
$L_{0.3-8} (\times 10^{38} \text{ erg s}^{-1})$	6.7

Various mechanisms can produce a broken power-law profile in the $\log N(>S) - \log S$ curve. The break may be caused by a pile-up of systems at a particular luminosity; in particular, it may be due to a population of neutron-star X-ray binaries (Sarazin et al. 2000) with a mass-transfer rate at or just above the Eddington limit, i.e., with bolometric luminosities $\sim 2 \times 10^{38} \text{ erg s}^{-1}$. Aging of a population of X-ray binaries born during a starburst episode can also produce a luminosity break in the $\log N(>S) - \log S$ curve (Wu 2001; Wu et al. 2001). In this model, the initial distribution has a power-law profile; as the bright, short-lived systems die, a break is created, moving gradually to lower luminosities with time. Pile-up of neutron-star X-ray binaries is a likely cause of the luminosity break in the $\log N(>S) - \log S$ curves of elliptical galaxies, where active star formation is absent. Population aging is a more likely mechanism for spiral galaxies, in particular those that have had tidal interactions with their satellites in the recent past (Wu 2001; Wu et al. 2001).

We have shown in Sect. 3 that the sources in the nuclear region of M83 and those in the disk appear to have different luminosity distributions. One of the obvious

features in the $\log N(>S) - \log S$ curve of the disk sources is a kink, located roughly at the Eddington luminosity of accreting neutron stars (if a distance of 3.7 Mpc is assumed). The slopes are approximately -0.6 and -1.3 at the low- and high-luminosity end, respectively. When we consider only the sources inside the $60''$ central region (which includes the nucleus and the stellar bar, but not the spiral arms), we obtain a simple power-law distribution with a slope of -0.8 (Fig. 3). This implies that the population of sources in the inner regions (nucleus and bar) has a larger relative fraction of bright sources than the disk population.

The situation is different for example in the spiral galaxy M81, where most bright sources are found in the galactic disk instead of the nuclear region (Tennant et al. 2001). If the flatness of the slope in the $\log N(>S) - \log S$ curve is an indicator of recent star formation, the difference in the spatial distribution of the brightest sources in M83 and M81 is simply a consequence of the fact that M83 has a starburst nucleus while star formation in galaxies such as M81 is presently more efficient in the galactic disk. With this interpretation, the current star formation rate in the disk of M83 would be intermediate between the rate in the disk of M81 (slope of -0.5 at the high-luminosity end) and in the bulge of M31 (slope of -1.8).

6.2. Nuclear region

The distribution of bright, young star clusters suggests that the most vigorous star formation is concentrated in a semi-circular annulus $\simeq 7''$ (≈ 130 pc) South-West of the IR photometric nucleus. From the colour distribution of the star clusters, it is inferred that star formation first started at the southern end of the ringlet about 10–30 Myr ago (Thatte et al. 2000; Harris et al. 2001), and has since propagated towards the currently more active northern end, where the age of most young stellar clusters is $\lesssim 5$ Myr. The youngest clusters are found along the outer edge of the ringlet, indicating that the star-formation front is presently propagating outwards (Harris et al. 2001).

The starburst nucleus of M83 was unresolved in all X-ray observations before *Chandra*; therefore, no comparisons between observations in the X-rays and in other wavelengths had been possible. Overplotting the *Chandra* brightness contours in the 0.3–8.0 keV band on the *HST*/WFPC2 multi-colour images (Fig. 11) helps to shed light on the relative spatial distribution of the X-ray and optical emission. For instance, although there is a general correlation, the optical emission is more strongly concentrated around the IR photometric nucleus and along the star-forming ring, while the X-ray emission is more uniformly distributed. There is also extended X-ray emission South-West of the star-forming arc, along the direction of the main galactic bar, and towards the North-West, across the dust lane, in a direction perpendicular to the bar. Discrete X-ray sources and unresolved emission are also found to the East of the IR photometric nucleus, not

associated with any bright optical regions with currently active star formation. This may be due to the fact that the optical emission traces the bright young stellar clusters and OB associations, while the X-ray emission is in general associated with remnants of stellar evolution such as accreting compact stars and supernovae.

The HST image shows that the IR photometric nucleus is strongly extinguished in the UV. The X-ray spectrum of the corresponding *Chandra* source (No. 43 in Table A.1) does not allow a precise determination of the absorption column density, but it constrains it to be $< 2.4 \times 10^{21}$ cm $^{-2}$ (Table 3). From the relation between the absorption column density n_{H} and the visual extinction A_V (Predehl & Schmitt 1995), this implies that the source has a visual extinction $A_V < 1.3$ mag. An extinction $A_V = 0.9$ mag has been deduced from IR observations (Thatte et al. 2000).

Unresolved soft emission extends for $\gtrsim 15''$ ($\gtrsim 270$ pc) to the South-West, West and North-West, outside the star-forming arc; the unresolved hard X-ray emission appears instead to be confined in the region between the IR photometric nucleus and the star-forming arc (Fig. 4, bottom right panel), and may perhaps extend to the North-West for $\lesssim 10''$ (≈ 180 pc). The X-ray spectrum of the unresolved component shows strong emission lines, typical of emission from optically-thin thermal plasma at $kT \approx 0.6$ keV. Above-solar abundances of Ne, Mg, Si and S are required to fit the spectrum, while Fe appears to be underabundant. This suggests that the interstellar medium in the starburst nuclear region has been enriched by the ejecta of type-II supernova explosions. A high C abundance and a high C/O abundance ratio can be the effect of radiatively-driven winds from metal-rich massive stars ($M \gtrsim 40 M_{\odot}$) in their Wolf-Rayet stage (Gustafsson et al. 1998; Portinari et al. 1998). Both effects are likely to be present in the nuclear region.

Four discrete sources are resolved along the star-forming arc. The brightest of them (No. 44 in Table A.1) is located near the southern end of the arc, where star formation started ≈ 10 –30 Myr ago (Harris et al. 2001). The other three sources (Nos. 35, 37 and 40) are towards the northern end of the arc, where star formation started more recently ($\lesssim 5$ Myr ago); source No. 35 is approximately coincident with the location of SN 1968L, a type-II supernova (Wood & Andrews 1974).

6.3. Black-hole candidates

Active galactic nuclei (AGN) are often found to have power-law X-ray spectra. If a thermal blackbody component is present, it peaks at energies $\lesssim 0.1$ keV and does not dominate in the 0.3–8.0 keV band. Black-hole X-ray binaries in hard spectral states also have single power-law spectra in the 0.3–8.0 keV band. When they are in the soft spectral state, instead, their X-ray spectra consist of a strong thermal blackbody component, with a temperature of about 1 keV, and a power-law tail, usually steeper than the power law in the hard state.

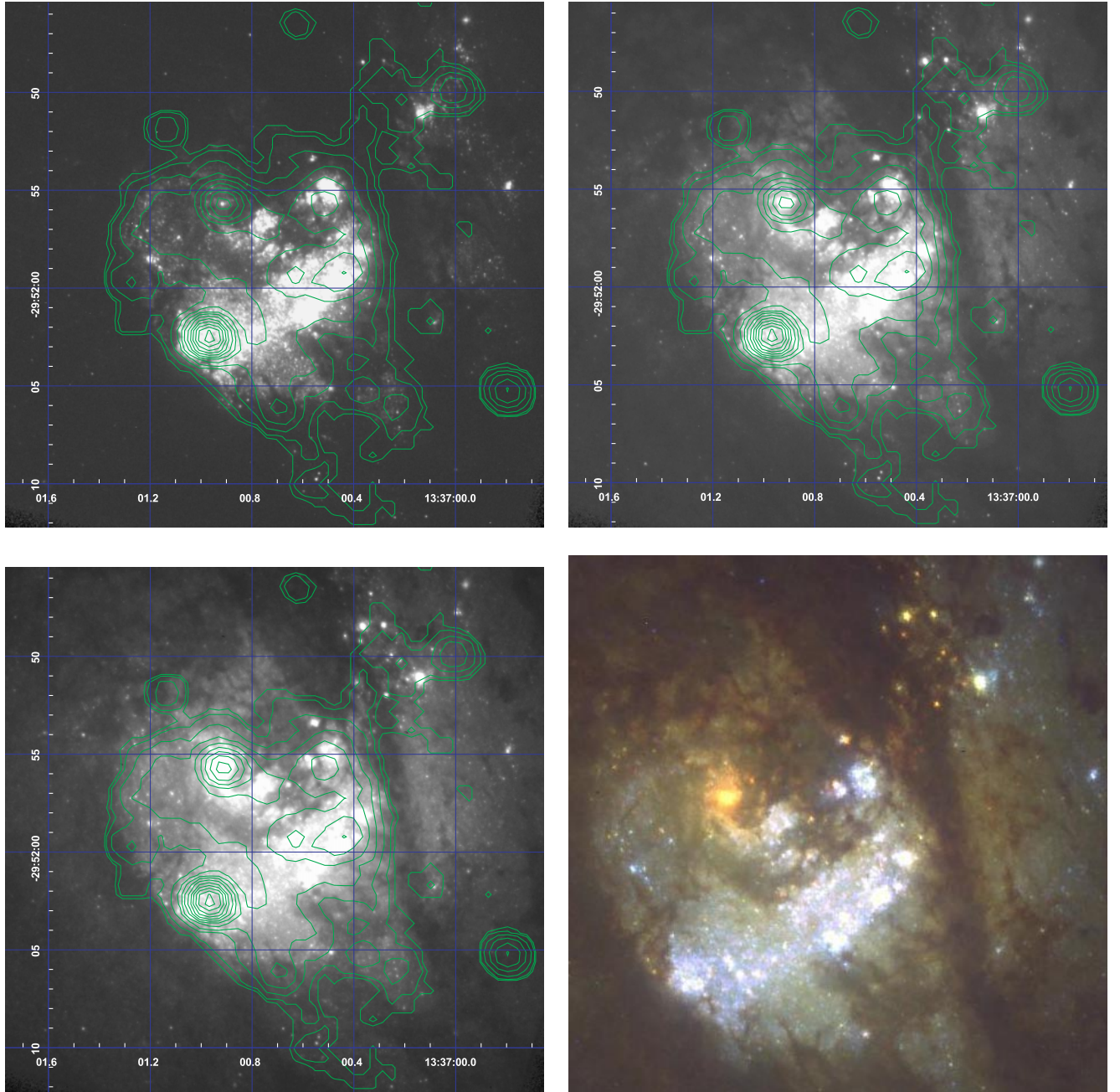


Fig. 11. The contours of the 0.3–8.0 keV emission in the nuclear region (smoothed with a $1''.5 \times 1''.5$ boxcar kernel) are overplotted on the *HST*/WFPC2 images in the F300W ($\approx U$; top left panel), F547M ($\approx V$; top right) and F814W ($\approx I$; bottom left) broad-band filters. A three-colour *HST*/WFPC2 image is also shown for comparison (bottom right, from Harris et al. 2001). The *HST* images, taken on 2000 April–May, were obtained from the STScI public archive. North is up, East is left.

The IR photometric nucleus has a power-law X-ray spectrum consistent with either those of accreting supermassive black holes in AGN, or those of stellar-mass black-hole candidates in X-ray binaries, in the hard state. The mass associated to the source is estimated, from stellar kinematics, to be $\approx 10^7 M_{\odot}$ (Thatte et al. 2000). If the source contains a supermassive black hole, analogous to those found in the nuclei of common Seyferts and quasars, and if the X-ray emission is powered by accretion, its luminosity ($L_x \simeq 3.2 \times 10^{38} \text{ erg s}^{-1}$ in the 0.3–8.0 keV band) is well below the Eddington limit; therefore, M83 is not in an AGN phase in the present epoch.

In the most accepted scenario, short-lived massive stars are the progenitors of stellar-mass black-hole candidates. Thus, some of the discrete X-ray sources in the nuclear region (excluding possible supernova remnants and the IR nucleus itself) may be high-mass black-hole X-ray binaries. Source No. 44 is a likely black-hole candidate, end product of the most recent starburst episode in the region (age < 30 Myr): its unabsorbed luminosity $\gtrsim 2.4 \times 10^{38} \text{ erg s}^{-1}$ in the 0.3–8.0 keV band places it above the luminosity of a neutron star accreting material at the Eddington rate.

Although the two brightest nuclear sources, Nos. 43 and 44, have comparable luminosity, and they are probably both powered by accretion onto a black hole, their spectral properties are different. The hard power-law photon index ($\Gamma < 1.5$) in the spectrum of the photometric nucleus and the kinematic properties of the stars around it suggest that it is a supermassive black hole. The other source has a much softer power-law photon index ($\Gamma > 2.5$) consistent with the spectrum of a stellar-mass black-hole candidate in the soft state. The present data are not sufficient to determine whether or not a disk-blackbody component is also present.

We can compare these two nuclear black-hole candidates with the brightest X-ray source in the M83 field, the *ROSAT* HRI source H30, which is located ≈ 4.5 (~ 5 kpc) away from the nucleus. Immler et al. (1999) suggested that H30 is also a strong black-hole candidate, because its luminosity is well above the Eddington limit for a $1.5-M_{\odot}$ compact star. (The source is still super-Eddington after accounting for the smaller distance to M83 assumed in this work.) Its spectrum can be fitted equally well with various models (Table 5). The most likely physical interpretation is that it is dominated by a steep ($\Gamma \approx 2.5$) power-law component, produced by Comptonisation of a soft blackbody component. The current data do not allow a simultaneous determination of the absorbing column density and of the temperature of the blackbody component. If the blackbody temperature $T_{\text{bb}} \ll 0.2$ keV, the total column density $n_{\text{H}} \approx 2.5 \times 10^{21} \text{ cm}^{-2}$. In the other extreme case, for $n_{\text{H}} = 4 \times 10^{20} \text{ cm}^{-2}$ (no intrinsic absorption), $T_{\text{bb}} \approx 0.25$ keV. An accurate determination of the optical extinction of a possible optical counterpart would constrain the temperature of the blackbody component in the X-ray spectrum, and hence the mass of the accreting object. This is left to further work.

The spectrum of H30 can also be well fitted with an optically-thin thermal plasma model (bremsstrahlung emission from completely ionised plasma at $kT \approx 2.5$ keV), consistent with a luminous supernova remnant. However, this latter possibility is much more unlikely because the source has shown variability during the *ROSAT* HRI observations and over the timespan of the *Chandra* observations. Moreover, no X-ray emission lines are detected in the spectrum, but the best-fit temperature is too low for the plasma to be completely collisionally-ionised. This would imply a metal abundance $\lesssim 0.1$ times the solar value (we have estimated it by fitting an absorbed Raymond-Smith model in XSPEC). Alternatively, the gas could be photo-ionised. Finally, a simple disk-blackbody spectrum with colour temperature of the inner accretion disk $T_{\text{in}} \approx 0.9$ keV, although physically unlikely, cannot be ruled out with the current data.

7. Summary

We analysed ACIS S3 data of the *Chandra* observation of M83. The starburst nuclear region is resolved in X-rays for the first time. Eighty-one point sources are detected above

$3.5\text{-}\sigma$. The sources are highly concentrated in the nuclear region, and 15 of them are found within the inner $16''$ region. One strong source coincides with the IR photometric peak, which is believed to be one of the two dynamical nuclei of the galaxy. We detect unresolved emission but no point-like sources (at a $2.5\text{-}\sigma$ level) at the centre of the outer optical isophote ellipses, where another dynamical nucleus is suspected to be located.

About 50% of the total emission in the nuclear region is resolved into discrete sources. The unresolved emission is extended outside the star-forming arc, both along the direction of the main galactic bar and perpendicular to it. In spite of the asymmetry, the azimuthally-averaged radial distribution of the unresolved emission appears to follow a King profile, with a central plateau, corresponding to the region inside the outer dust ring seen from IR observations, and no central cusp. The spectrum of unresolved emission shows strong emission lines, characteristic of an optically-thin thermal plasma at a temperature of ≈ 0.60 keV. We estimate that $\approx 70\%$ of the unresolved emission (35% of the total) is due to truly diffuse plasma, with the rest (15% of the total) coming from faint, unresolved point-like sources and photons in the wings of the PSF outside the detection cells of the resolved sources.

A much better fit to the diffuse emission is obtained when we assume higher metal abundances for selected elements: C (as expected if the interstellar medium in the nuclear region is strongly enriched by winds from massive Wolf-Rayet stars), Ne, Mg, Si and S (as expected if the gas is enriched by supernova ejecta). The emission lines are redshifted, implying projected radial velocities $\approx 7000 \text{ km s}^{-1}$.

Separating the discrete sources inside and outside a $60''$ central region reveals that the two populations have different cumulative luminosity distributions. The $\log N(>S) - \log S$ curve of the sources outside this radius (i.e., the disk population) shows a kink at luminosities consistent with the Eddington limit for neutron stars, indicating that a substantial fraction of the X-ray binaries in the disk contains a neutron star. No such feature is seen for the sources inside the $60''$ radius (i.e., those located in the nuclear region and along the bar). The slope of the $\log N(>S) - \log S$ curve at its high-luminosity end is flatter for the nuclear population, implying a larger fraction of bright sources (possible black-hole candidates). We interpret this as evidence that star formation is currently more active in the nuclear region than in the disk.

Acknowledgements. We thank Reiner Beck, Roy Kilgard, Miriam Krauss, Casey Law, Oak-Young Park, Elena Pian, Allyn Tennant and Daniel Wang for helpful discussions and suggestions. We are particularly grateful to the referee (Stefan Immler) for his detailed comments, which helped improve the paper substantially. This work is partially supported by a University of Sydney Sesqui R & D Grant. KW acknowledges support from Australian Research Council through an Australian Research Fellowship.

Appendix A

Table A.1. M83 sources detected at $3.5\text{-}\sigma$ level in the 0.3–8.0 keV band, and respective counts in a soft, medium and hard band, whenever the sources are also detected at $3\text{-}\sigma$ level in that band.

No.	RA(2000)	Dec(2000)	net counts ^a	0.3–1 keV	1–2 keV	2–8 keV	notes
1	13 36 40.9	–29 51 11.0	64.2 ± 12.2		35.0 ± 08.6		
2	13 36 41.4	–29 50 44.6	260.9 ± 22.4	61.1 ± 11.9	138.3 ± 15.0	62.3 ± 14.0	
3	13 36 43.5	–29 51 06.8	350.4 ± 22.9	52.5 ± 09.7	169.5 ± 16.2	129.1 ± 14.8	H08
4	13 36 48.0	–29 53 24.5	48.3 ± 09.2		22.0 ± 06.4		
5	13 36 49.1	–29 52 58.3	264.8 ± 19.4	158.2 ± 15.5	93.1 ± 11.9		H12a
6	13 36 49.2	–29 53 03.4	102.5 ± 12.6	45.9 ± 08.7	46.3 ± 09.1		H12b
7	13 36 49.8	–29 52 17.3	32.3 ± 08.5	24.2 ± 07.5			
8	13 36 51.7	–29 53 34.9	96.4 ± 13.9	35.6 ± 09.4	42.9 ± 09.5	21.7 ± 07.0	H14
9	13 36 53.2	–29 53 25.2	35.4 ± 09.7	28.8 ± 08.6			
10	13 36 53.3	–29 52 42.6	30.6 ± 08.4	21.3 ± 06.9			
11	13 36 53.9	–29 48 47.9	37.4 ± 09.8	31.2 ± 08.8			
12	13 36 53.9	–29 51 14.5	73.0 ± 10.6	37.9 ± 07.9	26.2 ± 06.8		
13	13 36 55.0	–29 52 39.4	31.1 ± 07.8	25.4 ± 07.2			
14	13 36 55.2	–29 54 03.6	86.7 ± 11.6	38.0 ± 08.0	35.2 ± 07.8		
15	13 36 55.5	–29 55 10.1	286.3 ± 20.9	68.3 ± 11.6	134.9 ± 14.3	83.2 ± 12.2	H15
16	13 36 55.6	–29 53 03.5	40.1 ± 09.5				
17	13 36 56.2	–29 52 55.3	29.6 ± 07.5				
18	13 36 56.7	–29 49 12.2	287.8 ± 21.2	78.7 ± 11.3	137.8 ± 14.7	71.3 ± 12.5	
19	13 36 57.3	–29 53 39.6	469.5 ± 23.3	161.1 ± 14.1	195.5 ± 15.5	113.0 ± 12.5	
20	13 36 57.5	–29 47 28.3	76.8 ± 14.0		30.4 ± 09.0	29.3 ± 09.3	
21	13 36 57.9	–29 53 02.9	75.9 ± 10.6	60.2 ± 09.3			
22	13 36 57.9	–29 49 23.2	35.2 ± 08.3				
23	13 36 58.2	–29 51 24.5	25.3 ± 06.8				
24	13 36 58.2	–29 52 15.8	169.5 ± 16.3	97.7 ± 12.7	57.0 ± 10.5		
25	13 36 58.3	–29 48 33.0	106.4 ± 14.7		48.4 ± 10.1	34.0 ± 9.2	
26	13 36 58.4	–29 51 04.8	112.8 ± 12.5		50.5 ± 08.6	55.9 ± 09.2	
27	13 36 59.1	–29 53 36.4	22.2 ± 06.4	21.1 ± 06.3			
28	13 36 59.5	–29 49 58.9	1085.2 ± 35.4	357.3 ± 21.1	427.5 ± 22.4	300.4 ± 19.3	H17
29	13 36 59.5	–29 52 04.0	46.6 ± 12.2	43.9 ± 10.9			^(b)
30	13 36 59.8	–29 52 05.6	268.7 ± 21.0	93.4 ± 14.1	124.3 ± 14.0	54.7 ± 09.9	^(b)
31	13 37 00.0	–29 51 50.3	169.3 ± 22.5	60.9 ± 15.7	70.8 ± 14.6	47.7 ± 09.1	^(b)
32	13 37 00.1	–29 53 29.9	29.1 ± 07.1				
33	13 37 00.2	–29 52 06.9	62.3 ± 18.1	63.1 ± 16.5			^(b)
34	13 37 00.3	–29 52 05.4	60.0 ± 20.0	52.0 ± 19.2			^(b)
35	13 37 00.4	–29 51 59.3	325.4 ± 37.8	263.7 ± 36.2	81.1 ± 19.6		^(b)
36	13 37 00.4	–29 50 54.0	68.8 ± 10.9	70.3 ± 10.8			
37	13 37 00.5	–29 51 56.3	272.6 ± 39.0	196.7 ± 31.7	73.0 ± 23.0		^(b)
38	13 37 00.6	–29 51 46.8	57.2 ± 12.9		33.6 ± 09.9		^(b)
39	13 37 00.7	–29 53 19.8	309.0 ± 19.8	106.9 ± 11.9	122.8 ± 13.0	79.3 ± 10.7	
40	13 37 00.7	–29 51 59.3	181.1 ± 39.0	158.4 ± 33.3			^(b)
41	13 37 00.7	–29 52 04.1	111.7 ± 32.0	90.5 ± 27.5			^(b)
42	13 37 00.7	–29 52 06.0	168.6 ± 28.9		84.0 ± 16.3	60.0 ± 09.8	^(b)
43	13 37 00.9	–29 51 55.8	689.9 ± 40.1	201.2 ± 28.2	264.9 ± 24.0	238.1 ± 18.4	IR nuclear peak ^(b)
44	13 37 01.0	–29 52 02.7	1215.2 ± 44.9	556.0 ± 32.9	514.8 ± 28.5	144.5 ± 14.2	^(b)
45	13 37 01.1	–29 52 45.8	80.5 ± 11.0	41.0 ± 08.0	23.9 ± 06.8	18.8 ± 05.7	H21
46	13 37 01.1	–29 51 51.9	64.7 ± 15.8		53.4 ± 11.0		^(b)
47	13 37 01.2	–29 54 49.5	108.8 ± 12.7	106.7 ± 12.6			
48	13 37 01.3	–29 52 01.9	42.9 ± 09.5			35.3 ± 07.7	^(b)
49	13 37 01.3	–29 52 00.0	70.1 ± 12.8	39.8 ± 10.2	26.9 ± 08.1		^(b)
50	13 37 01.3	–29 51 36.7	60.8 ± 10.5			53.0 ± 09.7	
51	13 37 01.5	–29 53 26.6	379.3 ± 21.8	56.8 ± 09.6	244.6 ± 17.6	77.7 ± 10.5	H20
52	13 37 01.6	–29 51 28.2	511.1 ± 25.9	216.4 ± 17.4	199.1 ± 16.6	100.1 ± 12.0	H23

^a Exposure time = 49.497 ks.^b Contributing to the nuclear source H19, unresolved by *ROSAT*.

Table A.1. continued.

No.	RA(2000)	Dec(2000)	net counts ^a	0.3–1 keV	1–2 keV	2–8 keV	notes
53	13 37 01.7	−29 47 42.4	206.5 ± 19.1	22.7 ± 07.5	114.5 ± 13.8	70.3 ± 12.5	
54	13 37 01.8	−29 51 13.0	24.3 ± 07.3	24.7 ± 07.0			
55	13 37 02.0	−29 55 18.2	319.7 ± 20.0	103.3 ± 12.3	99.6 ± 11.4	117.0 ± 12.9	H22
56	13 37 02.2	−29 55 06.2	40.7 ± 08.7		19.3 ± 6.0		
57	13 37 02.2	−29 49 52.3	28.8 ± 07.5				
58	13 37 02.4	−29 51 26.2	75.6 ± 10.4	56.9 ± 09.4	17.8 ± 05.8		
59	13 37 02.5	−29 53 19.3	80.7 ± 10.5		42.3 ± 08.0	24.2 ± 06.4	
60	13 37 03.3	−29 52 26.9	45.9 ± 08.6		22.3 ± 06.2		
61	13 37 03.9	−29 49 30.2	300.9 ± 19.8	109.4 ± 12.3	121.3 ± 13.2	70.4 ± 10.4	
62	13 37 04.3	−29 54 03.8	1094.4 ± 36.1	330.6 ± 20.1	555.1 ± 26.1	208.4 ± 16.5	H26
63	13 37 04.4	−29 51 30.5	43.2 ± 08.2	20.8 ± 06.1			
64	13 37 04.4	−29 51 21.5	1431.1 ± 39.9	441.3 ± 23.1	718.7 ± 28.5	270.9 ± 17.9	H27a
65	13 37 04.7	−29 51 20.4	67.5 ± 10.7	23.5 ± 06.7	26.5 ± 07.8	20.6 ± 06.0	H27b
66	13 37 04.8	−29 48 51.1	29.5 ± 08.2				
67	13 37 05.5	−29 52 34.1	76.9 ± 10.2		32.4 ± 07.1	44.1 ± 08.0	
68	13 37 06.1	−29 55 14.7	35.9 ± 08.3	27.6 ± 07.3			
69	13 37 06.2	−29 54 44.4	27.1 ± 07.1	22.3 ± 06.4			
70	13 37 06.2	−29 52 32.1	89.5 ± 11.2	87.8 ± 11.1			
71	13 37 07.1	−29 51 01.6	679.6 ± 29.1	24.4 ± 07.1	286.5 ± 19.6	366.8 ± 21.4	
72	13 37 11.9	−29 52 15.6	29.1 ± 07.3	24.0 ± 06.7			
73	13 37 12.5	−29 51 40.0	30.8 ± 07.2				
74	13 37 12.6	−29 51 55.0	105.6 ± 12.6		41.8 ± 08.4	61.0 ± 09.9	
75	13 37 12.9	−29 50 12.2	36.5 ± 08.1	31.6 ± 07.7			
76	13 37 14.5	−29 51 49.0	95.3 ± 11.8		54.1 ± 09.1	25.7 ± 07.1	
77	13 37 14.7	−29 49 44.2	53.6 ± 09.0		25.2 ± 06.6		
78	13 37 16.4	−29 49 39.1	397.9 ± 23.9	95.1 ± 12.1	166.6 ± 15.9	134.8 ± 14.6	H29
79	13 37 17.2	−29 51 53.5	87.3 ± 11.0	59.1 ± 09.3	25.4 ± 06.9		
80	13 37 18.0	−29 52 11.8	37.9 ± 08.1	21.8 ± 06.2			
81	13 37 19.7	−29 51 31.7	66.4 ± 10.5		19.0 ± 05.9	45.9 ± 08.9	

^a Exposure time = 49.497 ks.

References

- Arnaud, K. 1996, in ASP Conf. Ser. 101, *Astronomical Data Analysis Software and Systems V*, ed. G. Jacoby, & J. Barnes, 17
- Côté, S., Freeman, K. C., Carignan, C., & Quinn, P. 1997, *AJ*, 114, 1313
- de Vaucouleurs, G. 1979, *AJ*, 84, 1270
- de Vaucouleurs, G., de Vaucouleurs, A., Corwin, H. Jr., et al. 1991, *Third Reference Catalogue of Bright Galaxies* (Springer: New York)
- Ehle, M., Pietsch, W., Beck, R., & Klein, U. 1998, *A&A*, 329, 39
- Elmegreen, D. M., Chromey, F. R., & Warren, A. R. 1998, *AJ*, 116, 2834
- Fabbiano, G., Zezas, A., & Murray, S. S. 2001, *ApJ*, 554, 1035
- Gallais, P., Rouan, D., Lacombe, F., Tiphène, D., & Vauglin, I. 1991, *A&A*, 243, 309
- Giacconi, R., Rosati, P., Tozzi, P., et al. 2001, *ApJ*, 551, 624
- Gustafsson, B., Karlsson, T., Olsson, E., Edvardsson, B., & Ryde, N. 1999, *A&A*, 342, 426
- Harris, J., Calzetti, D., Gallagher, J. S. III, Conselice, C. J., & Smith, D. A. 2001 [[astroph/0109076](#)]
- Immler, S., Volger, A., Ehle, M., & Pietsch, W. 1999, *A&A*, 352, 415
- Okada, K., Mitsuda, K., & Dotani, T. 1997, *PASJ*, 49, 653
- Pence, W. D., Snowden, S. L., Mukai, K., & Kuntz, K. D. 2001, *ApJ*, in press [[astroph/0107133](#)]
- Portinari, L., Chiosi, C., & Bressan, A. 1998, *A&A*, 334, 505
- Predehl, P., & Schmitt, J. H. M. 1995, *A&A*, 293, 889
- Prestwich, A. H. 2001, in *X-rays at Sharp Focus: Chandra Science Symp.*, ed. S. Vrtilik, E. M. Schlegel, & E. Kuhi, in press [[astroph/0108523](#)]
- Sandage, A., & Tammann, G. A. 1987, *A revised Shapley-Ames Catalog of Bright Galaxies*, 2nd ed. (Carnegie Institution of Washington Publication: Washington)
- Sarazin, C. L., Irwin, J. A., & Bregman, J. N. 2000, *ApJ*, 544, L101
- Schlegel, D. J., Finkbeiner, D. P., & Davis, M. 1998, *ApJ*, 500, 525
- Shirey, R., Soria, R., Borozdin, K., et al. 2001, *A&A*, 365, L195
- Shrader, C. R., & Titarchuk, L. G. 1999, *ApJ*, 521, L21
- Tennant, A. F., Wu, K., Ghosh, K. K., Kolodziejczak, J. J., & Swartz, D. A. 2001, *ApJ*, 549, L43
- Thatte, N., Tecza, M., & Genzel, R. 2000, *A&A*, 364, L47
- Tilanus, R. P. J., & Allen, R. J. 1993, *A&A*, 274, 707
- Trinchieri, G., Fabbiano, G., & Palumbo, G. G. C. 1985, *ApJ*, 290, 96
- Wood, R., & Andrews, P. J. 1974, *MNRAS*, 167, 13
- Wu, K. 2001, *PASA*, 18, 443
- Wu, K., Tennant, A. F., Swartz, D. A., Ghosh, K. K., & Hunstead, R. W. 2001, *ApJ*, submitted